Deflection Angle Detection of the Rotor and Signal Processing for a Novel Rotational Gyroscope

Dianzhong Chen and Zhongzhao Zhang(✉)

Communication Research Center, Harbin Institute of Technology, Harbin 150001, China
dc2el2@163.com, zzzhang@hope.hit.edu.cn

Abstract. Differential capacitance detection, a common high resolution proof mass displacement detection scheme, is adopted in the gyroscope to measure the rotor deflection angle by installing an electrode with four poles under the rotor disk, which forms four detection capacitors and opposite ones form a differential capacitance detection pair. Theoretical inference explains the approximately proportional relationship between the capacitance difference and the rotor deflection angle. Simulation in Ansys Maxwell verifies the inference and confirms the differential capacitance detection range of the rotor deflection angle to 0–1°, limited by linearity. A signal processing system is constructed, obtaining a DC output voltage proportional to the measured input angular speed. Experiment shows the fabricated gyroscope with the designed differential capacitance detection pairs exhibits excellent performance with the resolution and the bias stability of 0.1 °/s and 0.5 °/h, respectively.

Keywords: Rotational gyroscope · Differential capacitance detection pair

1 Introduction

Gyroscope, angular speed sensor, has found applications in areas such as navigation, attitude control of aircraft, stability control systems in cameras, game controllers, automotive electronics, for instance, electronic stability program (ESP) [1]. Vibratory gyroscope and rotational gyroscope are the two main categories, based on Coriolis principle and precessional principle, respectively [2, 3]. The former has inherent problem of cross-talk between drive-mode vibration and sense-mode vibration, which restricts the performance [4, 5]. Small volume rotational gyroscope, mainly including magnetically suspended gyroscopes (MSG) and electrostatically suspended gyroscopes (ESG), with a rotor processing a large moment of inertia, exhibits higher performance than vibratory gyroscope. Researches on rotor suspension structures [3, 6], driving schemes [7, 8], pick up circuits [9, 10] and control electronics [11–14] to MSGs and ESGs have been conducted to improve measurement accuracy. Stability of rotor suspension has become a major constraint for further performance improvement of MSGs and ESGs.

L. Meng and Y. Zhang (Eds.): MLICOM 2018, LNICST 251, pp. 216–226, 2018.
https://doi.org/10.1007/978-3-030-00557-3_23

To obtain stable rotor support, a contacting low-friction rotor support structure with a water-film bearing is designed in the proposed gyroscope [15]. When sensing an input angular speed, rotor will deflect a certain angle proportional to the angular speed under the act of Coriolis torque, magnetic self-restoring torque and damping torque [16]. Thus, the measurement accuracy of rotor deflection angle is the critical point that determines performance of the gyroscope. Differential capacitance detection is a classic scheme for proof mass displacement measurement and for the proposed gyroscope, rotor deflection angle is detected by four capacitors formed by the rotor disk and four sectorial poles on a detection electrode. Opposite capacitors form a differential capacitance pair and two pairs can measure the rotor deflection angle at any direction of the stator plane (which is also the rotor plane when no input angular speed acts on the gyroscope). The gyroscope structure is illustrated and the operational principle of the proposed gyroscope is explained in Sect. 2. From analysis in Sect. 2, it is known that when sensing an input angular speed, rotor deflects an angle proportional to the angular speed with small amplitude harmonic vibration. Section 3 explains the principle of differential capacitance detection and defines the measurement angle range limited by the linearity of differential capacitance detection through simulation in Ansys Maxwell. Section 4 introduces the signal processing system and in Sect. 5, performance parameters of the gyroscope are tested. Section 6 summarizes the paper.

2 Operational Principle of the Gyroscope

2.1 Structure Design

The structure of the fabricated gyroscope is illustrated in Fig. 1. Figure 1(a) is a cross-section view by SolidWorks with a top-view of the detection electrode with four poles and Fig. 1(b) is a photograph of the fabricated gyroscope with the upper bronze shell open. Rotor is composed of a ball by stainless steel at the center and a ring-shaped disk by 2J85 grade permanent magnet, magnetized at the parallel direction, glued to the great circle. The diameter of the rotor ball, which is equal with the inner diameter of the rotor disk is 3 mm. The outer diameter and the thickness of the rotor disk are 10.8 mm and 0.5 mm, respectively. The stator, with 12 ring-distributed poles, is of the same thickness with rotor disk. A stable rotating magnetic field is produced by the stator to drive the rotor to a rated spinning speed of 10000 rpm. With no input angular speed acting on (zero state), the rotor disk and the stator are parallel. A detection electrode with four poles is installed to the lower supporting pillar (Fig. 1(a)), parallel to the rotor disk at zero state (with a distance of 100 μm). Each pole and the rotor disk construct a capacitor, and opposite ones compose a differential capacitor pair. Conducting oil is filled in the cavity of the upper supporting pillar and modulation signal V_{mod} (2 V, 15 kHz) is added through the upper supporting pillar, conducting oil, rotor ball to differential capacitor pairs. Two differential capacitor pairs detect the rotor deflection angle at the rotor plane which is perpendicular to the measurand of the input angular speed. For gyroscope, a higher angular momentum (H), which is proportional to rotor spinning speed, will produce a larger Coriolis torque under the same input angular speed, thus leading to a larger sensitivity. To obtain a high H, a superhydrophobic

surface is fabricated on the rotor ball and deionized water is filled in the cavity of the lower supporting pillar to form a water-film bearing under centrifugal force when rotor is actuated. With the rated driving current, steady-state spinning speed of the rotor with a superhydrophobic surface increases 12.4% [15].

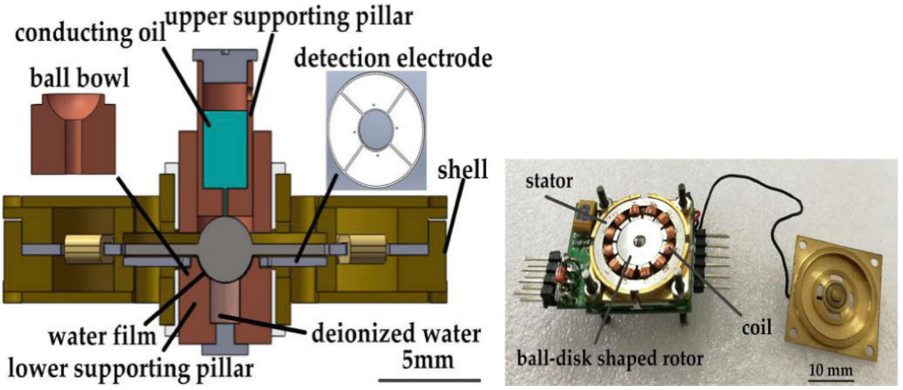

Fig. 1. (a) Cross-section view of the gyroscope; (**b**) Photograph of the gyroscope.

2.2 Sensing of Input Angular Speed

Schematic diagram for dynamics analysis of the gyroscope is as Fig. 2. Stator and rotor are fixed at the coordinates of $X_0Y_0Z_0$ and XYZ (without spinning motion), respectively. When the gyroscope senses an input angular speed at the $X_0Y_0Z_0$ plane, a proportional Coriolis torque M_G will act on the rotor, deflecting the rotor disk off the $X_0Y_0Z_0$ plane. For high relative magnetic permeability of the rotor disk and the stator (silicon steel sheets) compared with air, most of the magnetic energy is within the air gap. Tendency to keep total magnetic energy of the system as lowest produces a magnetic self-restoring torque (M_c) proportional to rotor deflection angle (φ), as inferred in [16]. Damping torque (M_d) at the X_0Y_0 plane exerted by the water-film bearing to the rotor ball is proportional to rotor precessional angular speed [16]. For high amplitude of H, nutation, which is low in amplitude and will attenuate fast, is neglected and dynamic equations for the rotor in the X_0Y_0 plane are as below:

$$M_{Gy} + M_{cy} + M_{dy} = \left(H\omega_x - H\dot{\beta}\right) - C_y\alpha - D_y\dot{\alpha} = 0, \tag{1}$$

$$M_{Gx} + M_{cx} + M_{dx} = \left(-H\omega_y - H\dot{\alpha}\right) + C_x\beta + D_x\dot{\beta} = 0, \tag{2}$$

where for the symmetrical structure of the gyroscope, letting self-restoring coefficient $C = C_x = C_y = M_c/\varphi$, damping coefficient $D = D_x = D_y = M_d/\omega$. Under step inputs of ω_x, ω_y with amplitudes of A_x, A_y, solutions of (1) (2) give:

$$\alpha(t) = \frac{H}{C}A_x + \frac{H}{C}\sqrt{A_x^2 + A_y^2}e^{-\frac{CD}{H^2+D^2}t}\sin\left(\frac{CH}{H^2+D^2}t + \varphi + \pi\right), \tag{3}$$

$$\beta(t) = \frac{H}{C}A_y + \frac{H}{C}\sqrt{A_x^2 + A_y^2}e^{-\frac{CD}{H^2+D^2}t}\cos\left(\frac{CH}{H^2+D^2}t + \varphi + \pi\right), \tag{4}$$

in which $\varphi = arctan(A_x/A_y)$. (3) (4) reflect dynamic response of the rotor responding to a step angular speed input (ω_x, ω_y) at the X_0Y_0 plane. Self-restoring torque (M_c) is a periodic restoring torque with the expression of $M_c = (C_1 + C_2\sin(4\pi ft + \psi))\varphi$ ($C_1 = 0.0219$, $C_2 = 0.0083$) [16]. Through inference, taking periodic self-restoring effect into account, expressions (3) (4) can be modified as [16]:

$$\alpha(t) = \frac{H}{C_1}\left(1 + \left(-\frac{C_2}{C_1}\right)\sin(4\pi ft + \psi)\right)\left[A_x + \sqrt{A_x^2 + A_y^2}e^{-\frac{C_1D}{H^2+D^2}t}\sin\left(\frac{C_1H}{H^2+D^2}t + \phi + \pi\right)\right], \tag{5}$$

$$\beta(t) = \frac{H}{C_1}\left(1 + \left(-\frac{C_2}{C_1}\right)\sin(4\pi ft + \psi)\right)\left[A_y + \sqrt{A_x^2 + A_y^2}e^{-\frac{C_1D}{H^2+D^2}t}\cos\left(\frac{C_1H}{H^2+D^2}t + \phi + \pi\right)\right], \tag{6}$$

in which $C_2/C_1 = 0.0083/0.0219 = 0.379$, f (167 Hz) is the driving frequency. Expressions (5) (6) indicate that the rotor will spiral at the angular speed of $C_1H/(H^2 + D^2)$ with the radius attenuation rate of $C_1D/(H^2 + D^2)$, to a dynamic equilibrium position of ($\alpha = HA_x/C_1$, $\beta = HA_y/C_1$) with harmonic angular vibration at the frequency of $2f$ within the range of C_2H/C_1^2. Thus, it can be concluded that dynamic equilibrium deflection angles α, β are proportional to measurands of input angular speeds ω_x, ω_y.

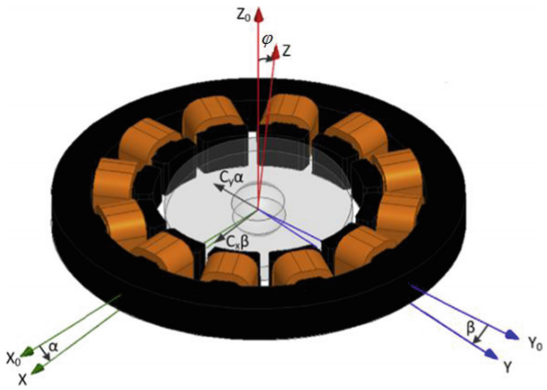

Fig. 2. Schematic diagram for dynamics analysis of the gyroscope.

3 Deflection Angle Detection by Differential Capacitance Pairs

Capacitive detection is adopted in the design and four poles on the electrode under the rotor disk form four capacitors with the disk. Two capacitors in X_0 or Y_0 direction form a detection pair. The detection schematic diagram is shown in Fig. 3. The inner radius R_i, outer radius R_o of the sector pole are the inner and outer radii of the rotor disk. The central angle of one pole, the distance between the pole and the rotor are set as $2\theta_0$ and h. When the rotor deflect an angle of small value $\vec{\varphi} = \alpha\vec{Y} + \beta\vec{X}$, letting $g(\theta) = \alpha cos\theta + \beta sin\theta$, the expression of C_{X^+} and C_{X^-} are:

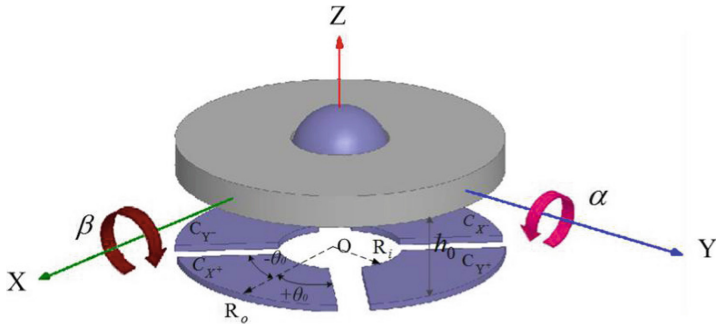

Fig. 3. Capacitive detection schematic diagram.

$$C_{X^+} = \varepsilon \int_{-\theta_0}^{\theta_0} \int_{R_i}^{R_o} \frac{r\,d\theta\,dr}{h_0 - r g(\theta)} = \varepsilon \int_{-\theta_0}^{\theta_0} \left[\frac{R_o - R_i}{-g(\theta)} - \frac{h_0}{g^2(\theta)} \ln \frac{h_0 - R_o g(\theta)}{h_0 - R_i g(\theta)} \right] d\theta, \tag{7}$$

$$C_{X^-} = \varepsilon \int_{-\theta_0}^{\theta_0} \int_{R_i}^{R_o} \frac{r\,d\theta\,dr}{h_0 + r g(\theta)} = \varepsilon \int_{-\theta_0}^{\theta_0} \left[\frac{R_o - R_i}{g(\theta)} - \frac{h_0}{g^2(\theta)} \ln \frac{h_0 + R_o g(\theta)}{h_0 + R_i g(\theta)} \right] d\theta. \tag{8}$$

Expanding expressions (7) (8) with Taloy's series gives:

$$\begin{aligned} C_{X^+} &= \varepsilon \int_{-\theta_0}^{\theta_0} \sum_{n=2}^{\infty} \frac{R_o^n - R_i^n}{n h_0^{n-1}} g^{n-2}(\theta) d\theta \\ &= \varepsilon \left[\frac{\theta_0 (R_o^2 - R_i^2)}{h_0} + \frac{R_o^3 - R_i^3}{3h_0^2} \int_{-\theta_0}^{\theta_0} g(\theta) d\theta + \frac{R_o^4 - R_i^4}{4h_0^3} \int_{-\theta_0}^{\theta_0} g^2(\theta) d\theta + \ldots \right], \end{aligned} \tag{9}$$

$$\begin{aligned} C_{X^-} &= \varepsilon \int_{-\theta_0}^{\theta_0} \sum_{n=2}^{\infty} (-1)^n \frac{R_o^n - R_i^n}{n h_0^{n-1}} g^{n-2}(\theta) d\theta \\ &= \varepsilon \left[\frac{\theta_0 (R_o^2 - R_i^2)}{h_0} + \frac{R_o^3 - R_i^3}{3h_0^2} \int_{-\theta_0}^{\theta_0} g(\theta) d\theta + \frac{R_o^4 - R_i^4}{4h_0^3} \int_{-\theta_0}^{\theta_0} g^2(\theta) d\theta - \ldots \right]. \end{aligned} \tag{10}$$

For α, β are of small values and $g(\theta) = \alpha cos\theta + \beta sin\theta$, items with integration of high orders of g(θ) are omitted. Then, Eqs. (9), (10) become:

$$C_{X^+} = \frac{\varepsilon\theta_0\left(R_o^2 - R_i^2\right)}{h_0} + \frac{\varepsilon\left(R_o^3 - R_i^3\right)}{3h_0^2}\int_{-\theta_0}^{\theta_0} g(\theta)d\theta = C_{X_0^+} + \frac{2\alpha\varepsilon\left(R_o^3 - R_i^3\right)\sin\theta_0}{3h_0^2}, \tag{11}$$

$$C_{X^-} = \frac{\varepsilon\theta_0\left(R_o^2 - R_i^2\right)}{h_0} - \frac{\varepsilon\left(R_o^3 - R_i^3\right)}{3h_0^2}\int_{-\theta_0}^{\theta_0} g(\theta)d\theta = C_{X_0^-} - \frac{2\alpha\varepsilon\left(R_o^3 - R_i^3\right)\sin\theta}{3h_0^2}, \tag{12}$$

where $C_{X_0^+}$, $C_{X_0^-}$ are the initial capacitance of C_{X^+}, C_{X^-} at zero state. Though the expressions of the two initial capacitance are the same, fabrication and assembling errors will cause inequality between them and the right expression in (11) and (12) are more accurate. Therefore, the changed capacitance caused by rotation angles of α and β are:

$$\Delta C_{X^+} = C_{X^+} - C_{X_0^+} = \frac{2\varepsilon\left(R_o^3 - R_i^3\right)\sin\theta_0}{3h_0^2}\alpha = G_d\alpha \tag{13}$$

$$\Delta C_{X^-} = C_{X^-} - C_{X_0^-} = -\frac{2\varepsilon\left(R_o^3 - R_i^3\right)\sin\theta_0}{3h_0^2}\alpha = -G_d\alpha \tag{14}$$

The coefficient of G_d is the amplification factor of differential capacitance. From expressions (13) and (14), it can be pointed out that the changed capacitance ΔC_{X^+} and ΔC_{X^-} are proportional to angle α and irrespective to β. The conclusion is based on the precondition that α, β are of small values and high order items in (9) and (10) are omitted. To identify the rotor deflection angle range, within which errors of linear approximation in (11) (12) are acceptable, capacitance differences between C_{X^+} and C_{X^-} under rotate_Y_angle (α) range of 0°–2° are simulated in ANSYS Maxwell (Fig. 4). It can be seen that the linearity of differential capacitance deteriorates with the increase of rotor deflection angle and the range of rotor deflection angle is limited to 0°–1°.

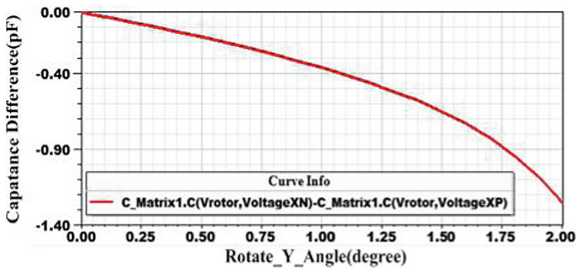

Fig. 4. Capacitance difference between C_{X^+} and C_{X^-} under rotate_Y_angle (α) from 0° to 2°.

4 Differential Signal Processing

To detect the capacitive change, a high frequency sinusoidal modulation signal V_{mod} (2 V, 15 kHz) is added to four capacitors through the rotor ball. Circuit through C_X pair (C_{X^+} and C_{X^-}) or C_Y pair (C_{Y^+} and C_{Y^-}) is induced to differential amplifier circuit. Proportional amplifier circuit is applied to amplify the signal to an appropriate amplitude. The signal detection block diagram is shown in Fig. 5. The processing system for C_X pair and C_Y pair are the same and the following derivation takes C_X pair, which senses X axis input angular speed, for example. In the circuit, resisters R_1, R_2, R_3, R_4 satisfy:

$$\frac{R_2}{R_1} = \frac{R_4}{R_3} = G_{op3}. \tag{15}$$

C_{f^+} and C_{f^-} are adjusted to satisfy:

$$\frac{C_{X_0^+}}{C_{f^+}} = \frac{C_{X_0^-}}{C_{f^-}}, \tag{16}$$

so that the zero state output voltage is zero. Then the output signal before HPF is:

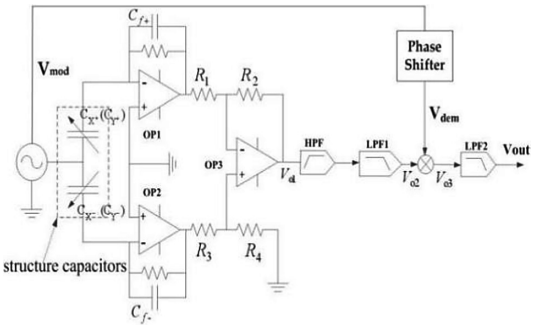

Fig. 5. Signal detection and processing system.

$$V_{o1} = G_{op3}V_{mod}\left(\frac{C_{X^+}}{C_{f^+}} - \frac{C_{X^-}}{C_{f^-}}\right) = G_{op3}V_{mod}\left(\frac{C_{X_0^+} + \Delta C_{X^+}}{C_{f^+}} - \frac{C_{X_0^-} + \Delta C_{X^-}}{C_{f^-}}\right) \tag{17}$$

Taking (13), (14), (16) into (17), the following equation can be derived:

$$V_{o1} = G_{op3}V_{mod}G_d\alpha\left(\frac{1}{C_{f^+}} + \frac{1}{C_{f^-}}\right) \tag{18}$$

Equation (18) reveals that an AC output voltage of, proportional to rotational angle α, is obtained. High pass filter (HPF) after V_{o1} filters out low frequency offset drift and 1/f noise first. Then low pass filter 1 (LPF1) filters out modulated signal of high frequency mechanical vibration (indicated in (5) and (6)) and nutation, obtaining V_{o2}. Afterwards, V_{o2} is demodulated by multiplier. Set the expression of V_{o2} as:

$$V_{o2} = GV_{mod}\alpha = G\alpha V_m \cos(\omega_c t + \varphi_0), \tag{19}$$

where $G = G_{op3}G_d\left(\frac{1}{C_{f^+}} + \frac{1}{C_{f^-}}\right)$, V_m is the amplitude of V_{mod} and ω_c is the angular frequency of V_{mod}. Demodulation signal V_{dem} after phase shifter is expressed as $V_m cos(\omega_c t + \varphi_1)$. Then, V_{o3} is:

$$\begin{aligned} V_{o3} &= V_{o2} \times V_{dem} = G\alpha V_m \cos(\omega_c t + \varphi_0) \times V_m \cos(\omega_c t + \varphi_1) \\ &= 0.5GV_m^2\alpha[\cos(2\omega_c t + \varphi_0 + \varphi_1) + \cos(\varphi_0 - \varphi_1)] \end{aligned} \tag{20}$$

It reveals that V_{o3} is composed of a DC signal, amplitude of which is sensitive to phase difference between V_{o2} and V_{dem}, and an AC signal with the frequency of ω_c/π. In the experiment, phase shifter is adjusted until maximum DC offset signal in V_{o3} is obtained. Finally, AC component in V_{o3} is filtered by LPF2, and V_{out} is a DC signal proportional to rotor deflection angle α in amplitude.

5 Measurement and Discussion

To observe the spectral characteristic of V_{out}, cut-off frequency of LPF2 is set as 50 Hz initially. Spectral analysis result is as Fig. 6, in which, 12 Hz, 167 Hz (f), 334 Hz ($2f$) components are observed. Parameters C_1, D have been identified through curve fitting in [16] to be 0.02017, 2.971×10^{-5}, respectively, and H (under rated driving speed of 10000 rpm) is calculated to be 2.784×10^{-4}. Then, rotor spiraling rate $(C_1H/(2\pi(H^2 + D^2)))$ indicated in expressions (5) (6) is calculated to be 11.4 Hz, which accounts for the first peak of spectral density in Fig. 6. It is analyzed in Sect. 2.2 that the rotor will vibrate at frequency $2f$ during precessional motion, which accounts for the third peak of spectral density in Fig. 6. Spectral component of the second peak (f) derives from asymmetrical fabrication error, which brings mechanical vibration at the driving frequency (f). To filter out these noises (12 Hz, 167 Hz, 334 Hz), cut-off frequency of LPF2 is set as 10 Hz finally. For LPF, a lower cut-off frequency will cause a longer response delay, thus increasing response time of the gyroscope.

Performance parameter test is conducted by putting the proposed gyroscope on a rate table. Input angular speeds within the measurement range of −30 °/s to 30 °/s (limited by the non-linearity of differential capacitance detection) with 5° intervals are given and output voltages are linear fitted in Matlab (Fig. 7(a)). Sensitivity and non-linearity within the measurement range are identified as 0.0985 V/(°/s) and 0.43%, respectively. Responses to exponentially-distributed input angular speeds from −0.00625 °/s to −1.6 °/s are tested and marked in Fig. 7(a). Analysis to these data reveals that the resolution of the gyroscope is 0.1 °/s. Bias stability test is done to the

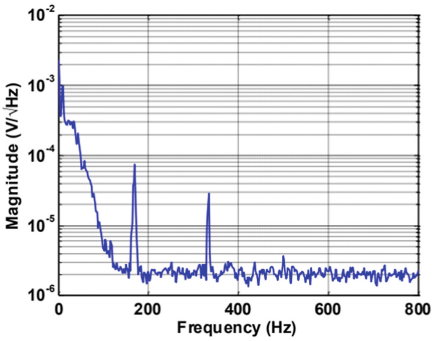

Fig. 6. Spectral density of V_{out}.

gyroscope (testing outputs of the gyroscope under 0 input angular speed) for half an hour. Allan derivation curve is plotted as Fig. 7(b), which identifies the bias stability to be 0.5 °/h.

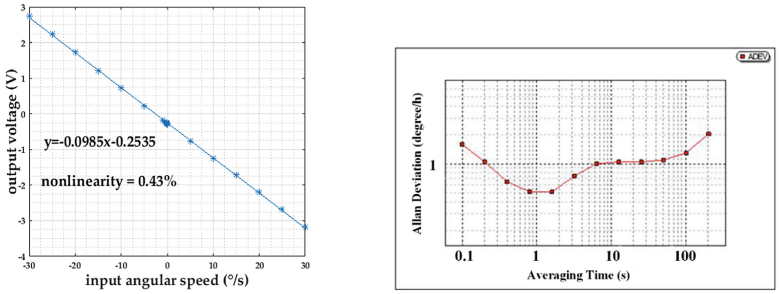

(a) (b)

Fig. 7. (a) Input-out characteristic of the proposed gyroscope; (b) Allan deviation curve.

6 Conclusions

Differential capacitance detection is adopted in the proposed rotational gyroscope with a specially designed ball-disk shaped rotor. A detection electrode with four sectorial poles is installed under the rotor disk to form 2 differential capacitance detection pairs, measuring the rotor deflection angle at the direction of the stator plane. Through theoretical inference, it is known that, firstly, capacitance difference of opposite detection capacitors (a differential capacitance detection pair) is approximately proportional to the rotor deflection angle at the perpendicular direction; and secondly, linear relationship of differential capacitance to rotor deflection angle deteriorates with the increase of the angle. Through simulation in Ansys Maxwell, non-linearity is acceptable when rotor deflection angle is within 1°, which restricts gyroscope measurement range to −30 °/s–30 °/s. A modulation signal (2 V, 15 kHz) is added to

differential capacitors to obtain an AC signal, proportional to the rotor deflection angle in amplitude. By multiplying the modulation signal after a phase shifter, AC signal is demodulated and a proportional output DC signal (V_{out}) is obtained, finally. Through spectral analysis, cut-off frequency of LPF before V_{out} is confirmed as 10 Hz. Gyroscope performance parameters of sensitivity, non-linearity, resolution, and bias stability are tested to be 0.0985 V/(°/s), 0.43%, 0.1 °/s, 0.5 °/h, respectively.

Acknowledgement. The work presented in this paper was supported by National Nature Science Foundation of China under Grant No. 91438205.

References

1. Saukoski, M., Aaltonen, L., Salo, T., Halonen, K.A.I.: Interface and control electronics for a bulk micromachined capacitive gyroscope. Sens. Actuators A **147**(1), 183–193 (2008)
2. Liu, K., et al.: The development of micro-gyroscope technology. J. Micromech. Microeng. **19**, 113001 (2009)
3. Xia, D., Yu, C., Kong, L.: The development of micromachined gyroscope structure and circuitry technology. Sensors **14**, 1394–1473 (2014)
4. Saukoski, M., Aaltonen, L., Halonen, K.A.I.: Zero-rate output and quadrature compensation in vibratory MEMS gyroscopes. IEEE Sens. J. **7**, 1639–1651 (2007)
5. Elsayed, M., Nabki, F., Sawan, M., El-Gamal, M.: A 5 V MEMS gyroscope with 3 aF/°/s sensitivity, 0.6°/$\sqrt{\text{hr}}$ mechanical noise and drive-sense crosstalk minimization. In: Proceedings of the 2011 International Conference on Microelectronics (ICM), Hammamet, Tunisia, 19–22 December 2011, pp. 1–5 (2011)
6. Cui, F., Liu, W., Chen, W.-Y., Zhang, W.-P., Wu, X.-S.: Hybrid microfabrication and 5-DOF levitation of micromachined electrostatically suspended gyroscope. Electron. Lett. **47**, 976–978 (2011)
7. Wu, H.M., Yang, H.G., Yin, T., Zhang, H.: Stability analysis of MEMS gyroscope drive loop based on CPPLL. In: Proceedings of the 2011 Asia Pacific Conference on Microelectronics and Electronics, Macao, China, 6–7 October 2011, pp. 45–48 (2011)
8. Mo, B., Liu, X.W., Ding, X.W., Tan, X.Y.: A novel closed-loop drive circuit for the micromechined gyroscope. In: Proceedings of the 2007 IEEE International Conference on Mechatronics and Automation, Harbin, China, 5–8 August 2007, pp. 3384–3390 (2007)
9. Feng, L.H., Zhang, Z.X., Sun, Y.N., Cui, F.: Differential pickup circuit design of a kind of Z-axis MEMS quartz Gyroscope. Procedia Eng. **15**, 999–1003 (2011)
10. Fang, R., et al.: A control and readout circuit with capacitive mismatch auto-compensation for MEMS vibratory gyroscope. In: Proceedings of the 11th IEEE International Conference on Solid-State and Integrated Circuit Technology (ICSICT), Xi'an, China, 29 October–1 November 2012, pp. 1–3 (2012)
11. Aaltonen, L., Halonen, K.A.I.: An analog drive loop for a capacitive MEMS gyroscope. Analog. Integr. Circuit Signal **63**, 465–476 (2010)
12. Cui, J., Chi, X.Z., Ding, H.T., Lin, L.T., Yang, Z.C., Yan, G.Z.: Transient response and stability of the AGC-PI closed-loop controlled MEMS vibratory gyroscopes. J. Micromech. Microeng. **12**, 1–17 (2009)
13. Yang, B., Zhou, B.L., Wang, S.R.: A precision closed-loop driving scheme of silicon micromachined vibratory gyroscope. J. Phys: Conf. Ser. **34**, 57–64 (2006)

14. Xiao, Q., Luo, Z.: Initial levitation of micromachined electrostatically suspended gyroscope with fuzzy hybrid PI controller. In: Proceedings of the International Conference on Control, Automation, Robotics & Vision, Phuket, Thailand, 13–15 November 2016 (2016)
15. Chen, D., et al.: Friction reduction for a rotational gyroscope with mechanical support by fabrication of a biomimetic superhydrophobic surface on a ball-disk shaped rotor and the application of a water film bearing. Micromachines **8**, 223 (2017)
16. Chen, D., et al.: A rotational gyroscope with a water-film bearing based on magnetic self-restoring effect. Sensors **18**(2), 415 (2018)